UNIVERSITY OF CALIFORNIA
Santa Barbara

Improved surface temperature estimates with MASTER / AVIRIS sensor fusion

A Thesis submitted in partial satisfaction
of the requirements for the degree of

Master of Arts

in

Geography

by

Erik Shane Philbert Grigsby

Committee in Charge:

Professor Dar A. Roberts, Chair

Professor Bodo Bookhagen

Professor James Frew

September 2014

The Thesis of
Erik Shane Philbert Grigsby is approved:

Professor Bodo Bookhagen

Professor James Frew

Professor Dar A. Roberts, Committee Chairperson

July 2014

Improved surface temperature estimates with MASTER / AVIRIS sensor fusion

by

Erik Shane Philbert Grigsby

To Mimar, for making this possible.

Acknowledgements

The research described in this thesis was initiated and made possible with funding from the NASA Student Airborne Research Program (SARP), and I am grateful to both Emily Schaller and Rick Shetter for their kind support and encouragement. I am indebted to both Christopher Scheele, who helped greatly at the onset of this work by drafting the initial code for TES, and Glynn Hulley, who was kind enough to help at the close of this work by contributing JPL code and resources to run the WVS method. I am forever grateful to Susan Ustin both for hiring me as a SARP mentor, and for helping to guide this thesis from research question inception through the writing of the final document. I also owe thanks to both Rose Dominguez and Jeff Myers at UARC for their assistance with MASTER calibration data, as well as Dr. David R. Smart and the USDA Specialty Crops Research Initiative (SCRI) for their role in collecting the ground measurements at Delano Vineyards. In addition to my patient thesis committee members James Frew and Bodo Bookhagen, I greatly appreciate Phaedon Kyriakidis for offering his time and insight. Finally, I am gratefully indebted to Dar Roberts for teaching, mentoring, and hosting me throughout my time at UCSB, for chairing this thesis, and above all for sharing with me how to actually do real science.

Abstract

Improved surface temperature estimates with MASTER / AVIRIS sensor fusion

Erik Shane Philbert Grigsby

Land surface temperature (LST) is an important parameter in many ecological studies, where processes such as evapotranspiration have impacts at temperature gradients less than 1 K. The current Root Mean Square Errors (RMSE) in standard MODIS and ASTER LST products are greater than 1 K, and for ASTER can be as large as 4 K for graybody pixels such as vegetation. Errors of 3 to 8 K have been observed for ASTER in humid conditions, making knowledge of atmospheric water vapor content critical in retrieving accurate LST. For this reason improved accuracy in LST measurements through the synthesis of visible-to-shortwave-infrared (VSWIR) derived water vapor maps and Thermal-Infrared (TIR) data is one goal of the Hyperspectral Infrared Imager, or HyspIRI, mission. The 2011 ER-2 Delano/Lost Hills flights acquired data with both the MODIS/ASTER Simulator (MASTER) and Airborne Visible InfraRed Imaging Spectrometer (AVIRIS) instruments flown concurrently. This study compares LST retrieval accuracies from the standard JPL MASTER temperature products produced using the Temperature Emissivity Separation (TES) algorithm,

and the Water Vapor Scaling (WVS) atmospheric correction method proposed for HyspIRI. The two retrieval methods are run both with and without high spatial resolution AVIRIS-derived water vapor maps to assess the improvement from VSWIR synthesis. We find improvement using VSWIR derived water vapor maps in both cases, with the WVS method being most accurate overall. For closed canopy agricultural vegetation we observed canopy temperature retrieval RMSEs of 0.49 K and 0.70 K using the WVS method on MASTER data with and without AVIRIS derived water vapor, respectively.

Contents

List of Figures

List of Tables

Chapter 1

Introduction

Kinetic temperature exerts a measurable effect on most physical processes, and is explicitly used as an input to model both plant water stress (Jackson et al. 1981) and evapotranspiration (Monteith et al. 1965, Allen et al. 1998). Water stress and evapotranspiration are of particular interest to farmers and water managers in arid drought prone regions such as California, where agricultural production was valued at $44.7 billon in 2012 (CDFA 2013). A 32.5% water delivery reduction has been predicted in the California Central Valley as a result of 2014 drought—a loss which will have an estimated total economic impact of $1.67 billon, including, direct, indirect and induced effects (Howitt et al. 2014). The socioeconomic effects of the current drought are predicted to be 50% more severe than those resulting from 2009 drought, and water reductions force difficult decisions for farmers: inefficient watering may bring a particular crop to harvest, at the cost of available water to other fields; water a crop too little and it will undergo cavitation and wilt, ruining

the harvest. Water stress affects the reproductive cycle of woody perennials—a group that includes the two largest irrigated crops in California, vineyards ($4.45 billion, 2012) and almond orchards ($4.35 billon, 2012) (CDFA 2013)—and can cause loss of crop productivity stretching over years that often requires redrafting or replanting. Accurate modeling of temperature and evapotranspiration provide farmers with robust estimates of water demand, enabling more conservative and efficient agricultural water use that reduces the human impact of drought.

While discrete *in situ* measurements are valuable tools for farmers, the size and scope of agriculture—10.28 million hectares and 80,500 farms in 2012 for California alone (CDFA 2013)—underscore the necessity for regional scale remotely sensed temperature estimates that are accurate. The accuracy of temperature estimates are particularly important for physical processes like evapotranspiration, which is mainly driven by the temperature gradient between the air and leaves, a gradient that can be less than 1 K for vegetation in semiarid ecosystems (Jarvis & McNaughton 1986). Current remotely sensed Land Surface Temperature (LST) estimates typically have errors on the order of 1 K when averaged over all surface types (Hulley et al. 2012); however, errors up to 4 K are typical for spectral graybodies such as vegetation (Gustafson et al. 2006), due to both uncertainty in emissivity and moister atmospheric profiles present over large contiguous vegetation patches. Even for targets with well known emissivity such

as water surfaces, errors as large as 3-8 K can occur due to humid conditions (Tonooka 2005), and robust atmospheric correction of thermal data is still essential in less humid mediterranean climates in order to provide operational data to farmers and resource managers.

1.1 Theoretical Background

Atmospheric correction of thermal data can be accomplished by a number of methods, however all methods focus on solving the same physical equation:

$$L_\lambda = [\epsilon_\lambda B_\lambda(T_s) + (1 - \epsilon_\lambda) * L_\lambda^\downarrow] * \tau_\lambda + L_\lambda^\uparrow \tag{1.1}$$

Where L_λ is the at sensor thermal radiance; ϵ_λ is an unknown emissivity; $B_\lambda(T_s)$ is the blackbody radiance at the surface temperature T_s; $L_\lambda^\downarrow$ and $L_\lambda^\uparrow$ are the downwelling and upwelling long wave radiance from the atmosphere; and τ_λ is the transmittance from the ground to the sensor. The surface temperature T_s is the only term that does not vary spectrally; the at sensor radiance L_λ is the only term that is empirically acquired as part of data collection. The $L_\lambda^\uparrow$ and $L_\lambda^\downarrow$ terms are atmospheric emittance terms that vary per pixel, and are determined by atmospheric composition and state (column water vapor, pressure, etc.), as is per pixel transmittance to the sensor.

Estimating LST from remotely sensed data is challenging in part because the emissivity of a surface, which varies spectrally, is required to invert the Planck function and retrieve LST (Zhengming & Dozier 1989). Solving for emissivity and LST simultaneously is an underdetermined problem, with N observations being used to solve for both a single temperature, and N emissivities (Realmuto 1990). Errors in emissivity estimation directly affects temperature retrieval accuracy during the Planck inversion, and add additional errors when correcting for downwelling atmospheric radiance that is reflected off of the surface. Current techniques such as the Temperature Emissivity Separation (TES) algorithm (Gillespie et al. 1998), have sought to constrain the emissivity solution space through the use of empirically established relationships related to the Min-Max Difference (MMD) in emissivity (Matsunaga 1994), or other related measures of spectral contrast. Unfortunately, these techniques are not effective over graybody pixels with low spectral contrast, such as vegetation, in part due to residual effects of incomplete atmospheric correction.

While well mixed atmospheric gasses such as CO_2 and O_3 can be estimated and corrected using regional estimates or model data from the National Center for Environmental Prediction (NCEP), significant challenges remain in correcting thermal imagery to account for column water vapor, an atmospheric constituent that varies temporally and is not well mixed across spatial scales (Gao & Goetz

1990). One solution to account for this variability is to directly invert and solve for physical water vapor within the atmosphere using radiative transfer code such as MODTRAN (Berk et al. 1987, 1998, 2005) to fit water absorption features within the individual spectra pixel-by-pixel (Green et al. 1993). Direct physical inversion for water vapor in the Thermal-InfraRed (TIR) portion of the spectrum is complicated both by the multisource nature of TIR emissions, and by low signal to noise ratios within the TIR; hence broadband sensors that include TIR channels such as the MODerate Resolution Imaging Spectrometer (MODIS) typically utilize the higher signal to noise ratios and single source nature of the Visible Short Wave InfraRed (VSWIR) channels to solve for total column water vapor. Since water absorption features within spectra are defined by their depth, width, and shape (Carrère & Conel 1993), high spectral resolution sensors such as the hyperspectral Airborne Visible/InfraRed Imaging Spectrometer (AVIRIS) are better able to retrieve total column water vapor relative to broadband sensors such as the MODIS ASTER Simulator (MASTER), which appears to underestimate total column water vapor (Roberts et al. 2012, Scheele et al. 2013). Given that uncertainty of column water vapor dominates as a source of atmospheric error when retrieving temperature from remotely sensed imagery (Hook et al. 2001), the fusion of broadband thermal imagery with shortwave hyperspectral imagery

opens exciting opportunities for improving temperature retrievals (Roberts et al. 2012).

1.2 Science Objectives and Relevance to HyspIRI

The National Research Council recommended HyspIRI mission, which combines a 213-channel VSWIR imaging spectrometer with an 8-channel TIR radiometer, would enable global simultaneous acquisition and synergy of hyperspectral VSWIR and TIR data at spatial resolutions comparable to Landsat (Roberts et al. 2012). In this paper, we assess the capabilities of HyspIRI like instrumentation in retrieving vegetation canopy temperature by comparing *in situ* leaf temperature measurements with temperatures retrieved using only TIR MASTER data, and temperatures retrieved using a synthesis of MASTER and AVIRIS remote sensing data. Specifically, we compare temperature estimates from the following five methods of temperature retrieval with *in situ* field data:

1. Single Band inversion using AVIRIS derived water vapor to estimate per pixel $L_\lambda^\downarrow$, $L_\lambda^\uparrow$ and τ_λ.

2. TES with $L_\lambda^\downarrow$, $L_\lambda^\uparrow$ and τ_λ terms derived from user supplied atmospheric terms, including a scene estimate of water vapor.

3. TES with per pixel $L_\lambda^\downarrow$, $L_\lambda^\uparrow$ and τ_λ terms supplied from AVIRIS derived water vapor, as in the single band case.

4. Water Vapor Scaling (WVS) method applied with NCEP estimates of water vapor used to scale $L_\lambda^\downarrow$, $L_\lambda^\uparrow$ and τ_λ terms derived from NCEP atmospheric profiles.

5. WVS applied using AVIRIS derived per pixel water vapor to scale $L_\lambda^\downarrow$, $L_\lambda^\uparrow$ and τ_λ terms generated from NCEP atmospheric profiles.

The WVS method was selected due to the increased accuracy that it offers in humid conditions where large uncertainties usually exist from remote sensing or model derived water vapor profiles (Tonooka 2005, Hulley et al. 2014), and also because it is the candidate algorithm for temperature retrievals for both MASTER and the upcoming HyspIRI mission. TES was selected since it is the current temperature retrieval algorithm in use for ASTER and MODIS; the MASTER-TES algorithm runs as a submodule to the WVS method, and comparison between the two showcases expected improvements between the two methods. Single Band inversion is the closest approximation to an unmodified application of Equation 1.1, and is used as a control between improvements in emissivity retrieval versus improvements in atmospheric correction. The differences in the Fields Of View (FOVs) in the broadband TIR radiometer and SWIR spectrometer on HyspIRI

will result in significant portions of the larger TIR swath that are not imaged by the VSWIR spectrometer; comparison of methods using NCEP and per pixel water vapor allow quantification of gains in temperature retrieval accuracy that can be expected within the overlapping scan area. These comparisons allow us to quantify the improvement that hyperspectral data bring to TIR temperature retrievals. They also provide insight into the magnitude and potential sources of remaining uncertainty in temperature retrievals. Validation of LST with *in situ* measurements showcases the potential benefits of a HyspIRI mission, both for LST accuracy in general and under challenging atmospheric conditions over vegetated surfaces. Accuracy assessment of temperature retrievals are important to know what physical processes we are able to model, as well as what new phenomena we will be able to explore using HyspIRI like sensors.

Chapter 2

Data and Methods

2.1 Study area

Our study focuses in a 15 ha Crimson seedless vineyard, a production table grape agriculture site in the San Joaquin Valley owned by Delano Vineyards. As part of an ongoing research study focused in remote sensing detection of vine water status (Alsina et al. 2013), the vineyard was split into two 7.5 ha blocks (North and South) and submitted to different watering regimes. Starting on April 8th 2011, and continuing throughout the growing season, the North block was irrigated to fully cover vine water demand while the South block was supplied with half the irrigation of the North control block, presenting a range of physiologic plant water status and canopy temperatures. The range of vegetation conditions, overall canopy closure, and presence of both *in situ* instrumentation and sampling were the primary factors that led us to select Delano Vineyards. The 2011 May 20th

afternoon flight included simultaneous data acquisition with both the AVIRIS and MASTER instruments that was temporally close to *in situ* field sampling of air and leaf temperature.

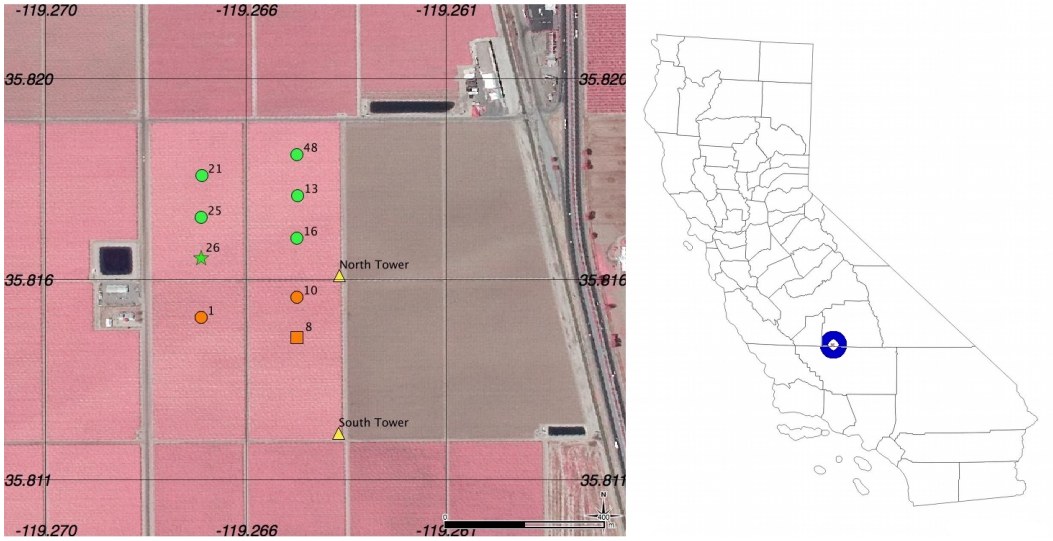

Figure 2.1: Field site at Delano Vineyards. Yellow triangles show locations of towers; numbered glyphs indicate data vines that were sampled. Vine 26 ('★') was sampled only during predawn; vine 8 ('□') was sampled only during the afternoon; all other data vines were sampled at both times. Vine glyphs are colored green for north block samples and orange for south block samples. The highway at the right of the image is California State Route 99 (SR 99).

2.2 Field Data

Leaf water potential and gas exchange were measured on the flight day both predawn and throughout the data acquisition flight windows, in 6 georeferenced vines per block (see Figure 2.1) using a Scholander chamber (Soilmoisture 3005,

Soilmoisture equipment corp. Santa Barbara, CA) and a a LiCor 6400 (LiCor Inc. Lincoln Nebraska, USA) respectively. The Licor instrument calculates the temperature gradient between the ambient air and a sampled leaf as part of its gas exchange analysis routine, using a fine wire thermocouple installed in the chamber to measure and record leaf temperature while taking a simultaneous measurement of the ambient air temperature. Two instrumented towers, one per block, were installed in the site to estimate surface energy fluxes using surface renewal. These towers recorded a number of variables, including air temperature by fine wire thermocouple, continuously for the week preceding and following the data flight at half hour intervals.

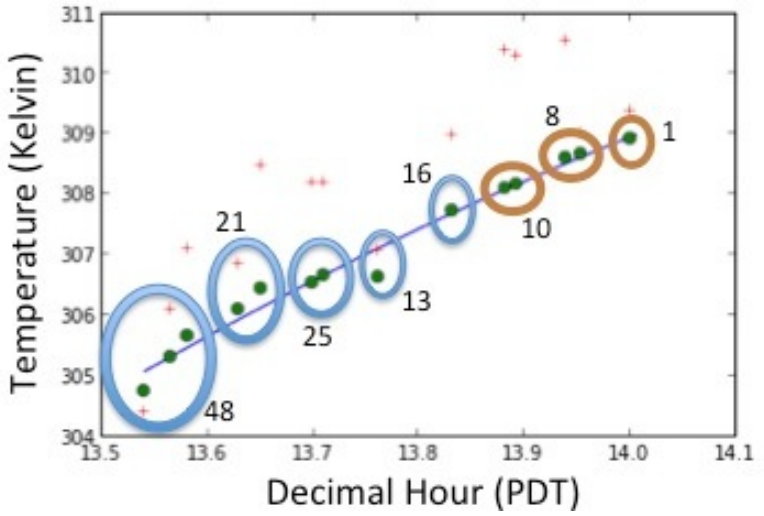

Figure 2.2: Leaf temperature (red crosses) and air temperature (green dots) as measured by the LiCor instrument during afternoon sampling on May 20th, 2011. Circled air temperature samples indicate sampling at a single data vine (text labels match Figure 2.1).

The *in situ* measurements of leaf temperature from the LiCor instrument (Figure 2.2) provide a close empirical estimate of canopy temperature, however a mismatch of 1 to 1.5 hours between the sampled measurements and the closest flight line prevented using the raw measures as validation data. The hour offset present between the end of the LiCor measurements and the data flight is because stomatal conductance measurements were taken coincident with the data flight and it was not feasible to take LiCor measurements simultaneously; the half hour of additional temporal variability is due to the time required to traverse and sample both the North and South data blocks. The differences in watering regimes between the North and South blocks introduces a spatial temperature gradient (Figure 2.3) imposed on top of the diurnal temperature trend present over the half hour sampling window. In order to separate the temporal and spatial temperature tends present in the LiCor leaf temperature measurements, and ultimately adjust leaf temperatures measurements forward in time to match the acquisition time of the remote sensing data, we modeled an aspatial diurnal temperature trend using tower data measurements (see Figure 2.4a).

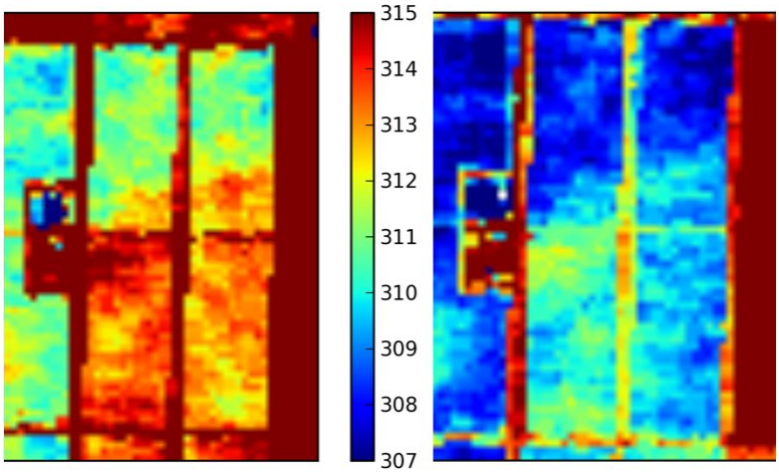

Figure 2.3: Spatial temperature gradient present at Delano field site, units are kelvin. The increasing trend of temperature from North to South is aligned with the North to South sampling order described in Figures 2.1 & 2.2, and is clearly present in the remote sensing data from both morning (*right*) and afternoon (*left*) MASTER data acquisitions. Temperatures shown retrieved using TES with AVIRIS water vapor as described in section 2.3.4

2.2.1 Diurnal temperature modeling

To model the aspatial diurnal temperature trend, we used the following equation:

$$K(t) = A * \cos((W * t) + S) + M + (D * (t - 140)) \tag{2.1}$$

Where A is the amplitude of the diurnal cycle (i.e., the range of the min/max temperature values); W is a shape parameters that corresponds to the width of the period; t is time in decimal julian day of the year; S is a offset shift that determines the alignment and timing of the daily min/max temperature trough/peak;

M is the mean daily temperature (centered on julian day 140); D is a linear term for the daily temperature trend; and $K(t)$ is the modeled temperature in Kelvin at time t. This function was fit to data from the North tower, which is positioned between the North and South data blocks (Figure 2.1), using a non-linear-least-squares-function (NLLSF) (Nelder & Mead 1965) to estimate parameters. The NLLSF function was seeded with initial parameter guesses of the mean temperature, amplitude, and daily temperature trend by taking the mean of the data set, the average difference between the min and max temperatures, and the best fit slope of the data set respectively. The window time selected for data input to the fitting function was three days (72-hours) prior and one day (24 hours) after the data flight; this range was chosen because it included four contiguous days about the data that shared similar atmospheric conditions—clear, low wind, and no clouds. The input data and result of the fit can be seen in Figure 2.4a.

Since the North Tower was positioned at the edge of the vineyard, with an ambient air temperature sensor fixed 1 meter above the vegetation canopy, the diurnal tower air temperature cycle was localized to a within canopy diurnal air temperature cycle using the LiCor measurements. The daily temperature trend D, and the timing of the daily minimum and maximum temperature as controlled by parameters S and W were assumed to be the same both within the canopy and at the North tower; the mean daily temperature M and daily temperature range

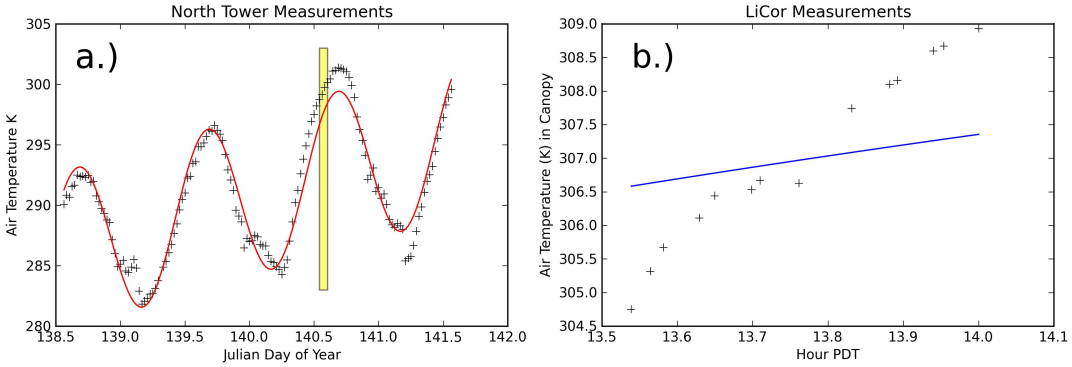

Figure 2.4: (a.) Diurnal model (red line) fit to North Tower data (crosses); model parameters as fit by NLLSF ($\chi^2_{red} = 1.76$) are as follows: $A = 6.565$, $W = 6.264$, $S = -1.570$, $M = 290.736$, $D = 3.125$. Yellow box is the time window for *in situ* LiCor measurements. **(b.)** Diurnal aspatial temperature model (blue line) for canopy air temperature; model parameters $W = 6.264$, $S = -1.570$, and $D = 3.125$ are fixed and taken from Figure 2.4a; model parameters $A = 9.62$, and $M = 297.605$ were determined by NLLSF fit to LiCor data. The modeled blue line represents the temporal trend only– LiCor data observations (crosses) encapsulate both a temporal trend and the spatial trend shown in Figure 2.3.

A were known to not be same from inspection of the LiCor predawn and afternoon measurements. Fixing D, S and W to the values calculated in Figure 2.4a, we reran the NLLSF on the predawn and afternoon LiCor air temperature measurements to estimate values of M and A appropriate to within the vegetation canopy. The resulting parameter estimates of Equation 2.1 can be seen in Figure 2.4b, and were used to estimate the aspatial (i.e., temporal) temperature trend within the canopy.

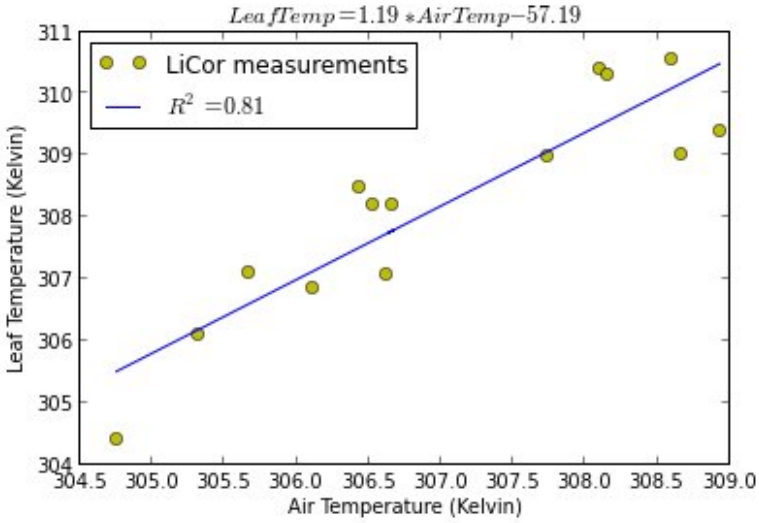

Figure 2.5: Regression of leaf and air LiCor temperature measurements.

2.2.2 Linking leaf and air temperature

While tower data measurements only include air temperature, and not leaf temperature, we found that the two temperature measurements were highly correlated throughout the sampling window and that air temperature can be used to predict canopy temperature using a simple linear regression ($R^2 = 0.81$, see Figure 2.5). We established this linear regression using the air and leaf temperatures from the LiCor instrument; since each pair of measurements are collocated in both time and space, we believe the relationship is robust across the spatial and temporal gradients. Using this regression to estimate leaf (and canopy) temperatures at the time of the data flight explicitly assumes that the leaf temperature to

air temperature relationship calculated using data collected from 1:30pm to 2pm is still valid at 3pm. Since there is no major shift in the heating regime over this time as measured by the towers (rnet), and since the time offset is never more than 90 minutes, we believe this to be a sound assumption.

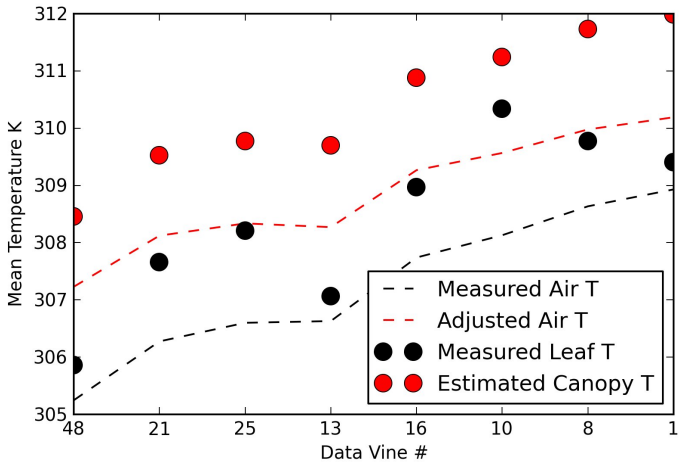

Figure 2.6: Black symbols are observations 1 to 1.5 hours prior to data flight. Red symbols are temperatures time adjusted to 15:01 PDT using Equation 2.1 with the coefficients listed in Figure 2.4b.

2.2.3 Adjusted field validation data

To capture the spatial variability in temperature within the data blocks shown in Figure 2.3, we calculated residuals between the *in situ* measurements of air temperature recorded by the LiCor instrument, and the modeled air temperatures shown in Figure 2.4b. These residuals were added back to the modeled air tem-

perature at the time of the data flight to yield spatially explicit air temperature estimates at 3:01pm PDT. The regression in Figure 2.5 was used to convert air temperature within the canopy to leaf temperature; these adjusted measures of leaf temperature shown in Figure 2.6 represent our best estimate of canopy temperature at the time of the data flights, and were used as independent verification data in assessing our remote sensing temperature retrievals.

2.3 Remote Sensing Data

The NASA ER2 passed over the Delano Vineyard field at 15:01 local time (PDT; 22:01UTC) on May 20th 2011 at an altitude of 8.3km carrying both the AVIRIS and MASTER instruments. The orthorectified and overlaid images in Figure 2.7 show the result of both the different sensor swath widths (FOVs) and spatial resolutions (IFOVs). The flight speed resulted in an oversampled area of interest, leading to higher effective spatial resolutions compared to the instrument IFOVs—6.9 meters for AVIRIS and 13.1 meters for MASTER. We found the MASTER georeferenced product to be highly spatially accurate over our field site, with the corners of the north and south data blocks in the MASTER imagery aligned to ground sampled GPS points with sub pixel accuracy and not in need of further spatial correction or georegistration.

Figure 2.7: MASTER and AVIRIS flightlines; yellow box is the field site shown in Figure 1. MASTER bands: $Red = 9, Green = 5, Blue = 3$; AVIRIS bands: $Red = 29, Green = 20, Blue = 11$

2.3.1 AVIRIS water vapor retrieval

We retrieved precipitable column water vapor for the AVIRIS flight line using the ACORN atmospheric correction software run in mode 1.5 with a tropical

atmosphere profile. The tropical atmosphere profile was used in ACORN because the starting surface temperature of this profile more closely matched the surface temperature of the *in situ* data, and the atmospheric conditions of the heavily irrigated central valley in May are better approximated by the tropical profile in MODTRAN than by the mid-latitude summer profile. Additionally, the mid-latitude summer profile was prone to saturate water vapor estimates over moist pixels due to the lower saturation vapor pressure that this cooler temperature profile provides. Liquid water within the canopy was also simultaneously retrieved in ACORN to avoid overestimation of water vapor from mixing of the adjacent liquid and vapor water absorption features (Gao & Goetz 1990). Both the 940nm and 1140nm water absorption features were used for the inversion, with aerosol path scattered radiance included within the fit. ACORN optimized visibility, the parameter that accounts for aerosols within ACORN, to a value of 20km from an initial estimate of 16km provided from the nearest airport in Bakersfield, CA.

Despite the higher spatial resolution of AVIRIS, higher accuracy georegistration within the MASTER data product led us to use MASTER as the authoritative basemap when coregistering the MASTER and AVIRIS datasets. To register the datasets we first resized the 6.9 meter pixels of the AVIRIS imagery and AVIRIS derived water vapor map to match the larger 13.1 meter MASTER pixels using pixel aggregate resampling. The resampled visible bands of AVIRIS were reg-

istered to the visible bands of MASTER applying pixel offsets to translate the AVIRIS image and align linear features present in the imagery. Specifically, the resampled AVIRIS data were shifted 2 pixels east and one pixel north in order to match the corners of the data blocks and align the roads. These same pixel offsets found in the visible AVIRIS imagery were used to translate and register the AVIRIS derived water vapor map.

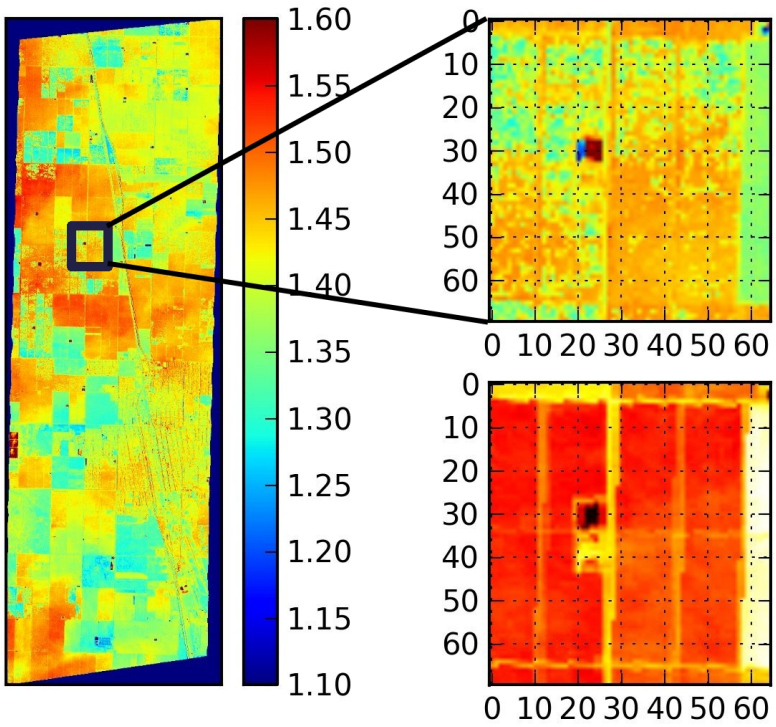

Figure 2.8: (left): AVIRIS derived water vapor; units are in grams of precipitable water. (right top): Subset of resampled AVIRIS water vapor over validation site; colors match left image. (right bottom): Matching subset of radiance image for band 44 of MASTER. Roads are noticeably hotter than the fields; pixel incremented grid overlaid over right images to allow comparison of registration between MASTER and AVIRIS.

2.3.2 Thermal Infrared data preprocessing

We selected five MASTER bands from the TIR for thermal temperature retrieval processing: bands 43 (8.62 μm), 44 (9.09 μm), 47 (10.64 μm), 48 (11.33 μm), and 49 (12.12 μm). These bands were selected to best approximate the HyspIRI proposed bands centered at 8.63 μm, 9.07 μm, 10.53 μm, 11.33 μm, and 12.05 μm. We excluded MASTER band 41 (7.81 μm) since it does not fall within an atmospheric window region; MASTER band 42 (8.18 μm) approximates the proposed 8.28 μm HyspIRI band but was excluded to reduce atmospheric error due to combined water vapor and methane absorption within the band. We used radiometrically corrected MASTER L1B data for determining at sensor radiance, and convolved atmospheric radiance terms using monochromator derived empirical Spectral Response Functions (SRFs) measured prior to the data flights at NASA Ames on May 11th, 2011.

2.3.3 Single band inversion

Temperature retrieval from thermal data consists of three broad steps: atmospheric correction of at sensor radiance to at ground emitted radiance, estimation of target emissivity, and inversion to physical temperature using estimated target emission and emissivity. The single band inversion method follows an initial correction routine similar to TES and WVS, but separates atmospheric correction

error from TES emissivity estimation error by bypassing the TES module and prescribing an *a priori* fixed value of the maximum spectral surface emissivity for one band. The maximum spectral graybody emissivity of vegetation ranges from 0.97 to 0.99, and since our pixels are smaller and less heterogeneous then either MODIS or ASTER, we set a value of 0.99 for maximum spectral emissivity in the initial atmospheric correction.

To correct sensor radiance to at ground radiance, we ran MODTRAN to generate 42 different atmospheric models, varying precipitable water vapor from 1.00 to 1.82 grams/cm^2 in 0.02 gram/cm^2 increments. The input parameters for MODTRAN runs were taken from the AVIRIS atmospheric correction detailed in section 2.3.1, with additional atmospheric constituents estimated from NCEP as appropriate. Each MODTRAN run yielded water vapor dependent values of $L_\lambda^\uparrow$, $L_\lambda^\downarrow$, and τ_λ from 8 μm to 14 μm at a spectral resolution of 1nm. After the MODTRAN models were convolved to the MASTER bands using the May 11th SRFs, we fit univariate splines between the different water vapor models, an approach that is a modification of the Green et al. (1991) method to generate reverse Look Up Table's (LUTs) for atmospheric correction; here we use the method to create forward LUT's in the thermal region.

We processed the MASTER TIR data using the following equation:

$$[(L_\lambda - L_\lambda^\uparrow)/\tau_\lambda] - (0.01) * L_\lambda^\downarrow = 0.99 * B_\lambda(T_s) \tag{2.2}$$

Where Equation 2.2 is identical to Equation 1.1, but assumes an initial value of $\epsilon_\lambda = 0.99$ for all bands. The $L_\lambda^\uparrow$, $L_\lambda^\downarrow$, and τ_λ values per pixel were estimated by looking up column water vapor from the corresponding AVIRIS water vapor pixel described in section 2.3.1, and retrieving the corresponding $L_\lambda^\uparrow$, $L_\lambda^\downarrow$, and τ_λ values from the thermal LUT's. Taking the per pixel hottest band as the closest to true surface temperature, we calculated the relative emissivity for the other bands assuming a physical temperature equal to the hottest band. The final per band temperatures were estimated by using the same $L_\lambda^\uparrow$, $L_\lambda^\downarrow$, and τ_λ values per pixel applied to Equation 1.1 with the calculated relative emissivities applied to reduce error in the reflected $L_\lambda^\downarrow$ component; the average of the Planck inversion temperatures for all 5 bands yielded the retrieved temperature.

2.3.4 Temperature and Emissivity Separation (TES)

The TES algorithm (Gillespie et al. 1998, Gustafson et al. 2006) uses the same initial procedure described in section 2.3.3, but solves for emissivity through the use of an empirical relationship that correlates spectral contrast between a specific set of bands and the minimum emissivity, ϵ_{min}, of laboratory measured surface

types as described in Baldridge et al. (2009) and Hulley & Hook (2009). The regression for MASTER bands 43, 44, 47, 48, and 49 is shown Figure 2.9, as well as in Equation 2.3 below:

$$\epsilon_{min} = 0.9921–0.74329 * MMD^{0.78522} \tag{2.3}$$

Where $MMD = Max(\epsilon_{\lambda}^{stand}) - Min(\epsilon_{\lambda}^{stand})$

Following an initial atmospheric correction with Equation 2.2, we calculated the standardized emissivity ($\epsilon_{\lambda}^{stand}$) by dividing the per pixel relative emissivities from section 2.3.3 by the pixel mean of those relative emissivities. We calculated the MMD and ϵ_{min} per pixel using Equation 2.3, and then used Equation 2.4 to solve for calibrated emissivity (ϵ_{λ}^{cal}):

$$\epsilon_{\lambda}^{cal} = \epsilon_{\lambda}^{stand} * [\epsilon_{min}/min(\epsilon_{\lambda}^{stand})] \tag{2.4}$$

Where $min(\epsilon_{\lambda}^{stand})$ is the minimum standardized emissivity for a pixel among all of the bands used for the correction. The ϵ_{λ}^{cal} were then used with Equation 1.1, and as in section 2.3.3, the average temperature from MASTER bands 43, 44, 47, 48, and 49 was considered the retrieved temperature. In addition to using the per pixel estimates of $L_{\lambda}^{\uparrow}$, $L_{\lambda}^{\downarrow}$, and τ_{λ} provided from the AVIRIS water vapor map, this procedure was applied to generate the JPL standard product. The JPL standard product is available for all MASTER flight lines and uses scene

estimated $L_\lambda^\uparrow$, $L_\lambda^\downarrow$, and τ_λ derived from MODTRAN with user supplied atmospheric parameters; we supplied matching parameters to the JPL standard product to facilitate comparison.

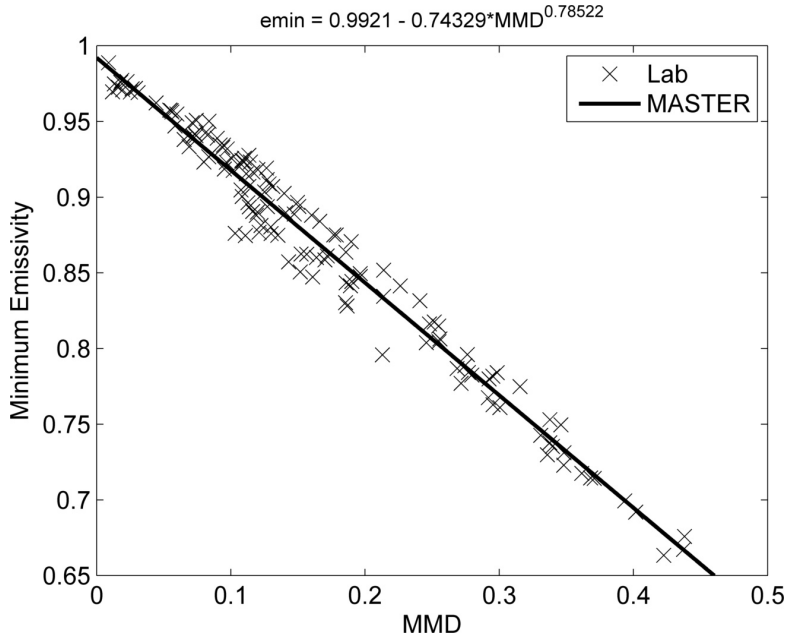

Figure 2.9: MMD empirical regression for MASTER bands 43, 44, 47, 48, and 49

2.3.5 Water Vapor Scaling (WVS)

To apply WVS to the Delano scenes, we modified the base $L_\lambda^\uparrow$, $L_\lambda^\downarrow$, and τ_λ terms of Equation 1.1 using Equations 2.5, 2.6, and 2.7 respectively:

$$L_\lambda'^\uparrow(\gamma) = L_\lambda^\uparrow(\gamma_1) * \frac{1 - \tau_\lambda'(\gamma)}{1 - \tau_\lambda(\gamma_1)} \tag{2.5}$$

$$L'^{\downarrow}_{\lambda}(\gamma) = a_\lambda + b_\lambda * L'^{\uparrow}_{\lambda}(\gamma) + c_\lambda * L'^{\uparrow}_{\lambda}(\gamma)^2 \tag{2.6}$$

$$\tau'_\lambda(\gamma) = \tau_\lambda(\gamma_1)^{\frac{(\gamma^{a_\lambda} - \gamma_2^{a_\lambda})}{(\gamma_1^{a_\lambda} - \gamma_2^{a_\lambda})}} * \tau_\lambda(\gamma_2)^{\frac{(\gamma_1^{a_\lambda} - \gamma^{a_\lambda})}{(\gamma_1^{a_\lambda} - \gamma_2^{a_\lambda})}} \tag{2.7}$$

Where 'γ_1' and 'γ_2' are constants set to 0.7 and 1, and a, b, and c are regression coefficients; an atmospheric term ($L^{\uparrow}_{\lambda}$, $L^{\downarrow}_{\lambda}$, or τ_λ) as a function of a subscripted γ_1 or γ_2 indicates the atmospheric term calculated using an amount of precipitable water vapor scaled by the corresponding constant. The band model parameter 'α_λ' and apparent surface brightness temperature 'T_{α_λ}' were determined using the Enhanced MultiChannel Water Vapor Dependent (EMC/WVD) split-window algorithm (Equations 2.8 and 2.9) as described in Tonooka (2005) and Hulley & Hook (2011):

$$\alpha_\lambda = p_\lambda + q_\lambda W + r_\lambda W^2 \tag{2.8}$$

$$T_{a_\lambda} = \alpha_{\lambda,0} + \sum_{k=1}^{n} \alpha_{\lambda,k} T_k \tag{2.9}$$

Where W is precipitable water vapor in grams/cm^2; n is the number of bands used in TES ($n = 5$); k is an assigned band number 1 through 5 for the corresponding band centered at wavelength λ; and p, q, and r are regression coefficients as

determined by from a global simulation model using NCEP model data (Tonooka 2001).

The WVS method takes per-band brightness temperatures at a given pixel calculated from Equation 2.9, and an estimate of water vapor over that pixel to generate band-dependent scaling factors to modify and scale the $L_\lambda^\uparrow$, $L_\lambda^\downarrow$, and τ_λ terms of Equation 1.1 to the $L_\lambda'^\uparrow(\gamma)$, $L_\lambda'^\downarrow(\gamma)$, and $\tau_\lambda'(\gamma)$ terms of Equations 2.5, 2.6, and 2.7. The per band and pixel WVS scaling factor 'γ' is calculated from the band model parameter 'α_λ' (Equation 2.8) and apparent surface brightness temperatures 'T_{α_λ}' using Equation 2.10:

$$\gamma = \frac{ln\left(\frac{\tau_\lambda(\gamma_2)^{\gamma_1{}^{\alpha_\lambda}}}{\tau_\lambda(\gamma_1)^{\gamma_2{}^{\alpha_\lambda}}} * \left(\frac{\frac{B_\lambda(T_{a_\lambda})-L_\lambda^\uparrow(\gamma_1)}{1-\tau_\lambda(\gamma_1)}}{\frac{L_\lambda-L_\lambda^\uparrow(\gamma_1)}{1-\tau_\lambda(\gamma_1)}}\right)^{\gamma_1{}^{\alpha_\lambda}-\gamma_2{}^{\alpha_\lambda}}\right)}{ln\left(\frac{\tau_\lambda(\gamma_2)}{\tau_\lambda(\gamma_1)}\right)} \tag{2.10}$$

The 'γ' WVS scaling factors were only computed over graybody targets to minimize emissivity effects, and were then interpolated over any bare pixels on the scene using an inverse distance weighting interpolation. In contrast to the $L_\lambda^\uparrow$, $L_\lambda^\downarrow$, and τ_λ values retrieved from interpolated LUT's as described in sections 2.3.4 and 2.3.3, and since the estimates of $L_\lambda^\uparrow$, $L_\lambda^\downarrow$, and τ_λ are scaled by water vapor separately, we used the same base $L_\lambda^\uparrow$, $L_\lambda^\downarrow$, and τ_λ estimates derived from MODTRAN run with NCEP inputs when deploying WVS.

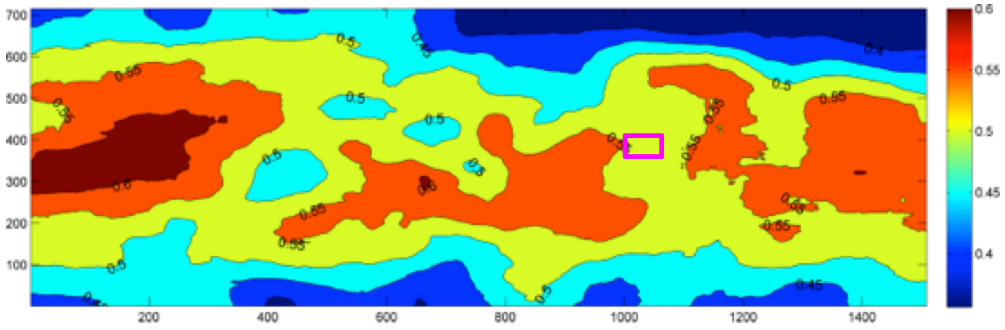

Figure 2.10: WVS scaling factor for MASTER band 44 using AVIRIS derived water vapor estimate; purple rectangle marks field validation site. The x-axis and y-axis coordinates are across track and along tract pixel coordinates for the MASTER sensor.

These scaling factors were applied to both 1 degree water vapor estimates provide by NCEP, and also to the 13.1 meter resolution water vapor maps that AVIRIS provided; the calculated 'γ' factor inputs provided by AVIRIS are shown in Figure 2.10 for MASTER band 44. Values less than 1 indicate that water vapor over the scene was overestimated by the NCEP data. Using an estimate of high resolution AVIRIS water vapor in the EMC/WVD equation improved the accuracy of these scaling factors. Following the application of scaling factors using Equations 2.5 through 2.10, temperature and emissivity was retrieved using the TES method as described in the HyspIRI TES ATBD (Hulley 2011).

Chapter 3

Results

The results of temperature retrievals from single-band inversion, TES, and WVS—with and without AVIRIS derived water vapor—are shown in Table 3.1 on page 31. We selected the JPL standard product as our baseline in comparing temperature retrieval improvements since it is available for all MASTER scenes, although the TES+WVS method will eventually replace stand-alone TES as the new JPL standard product. Our results show that there is a strong tendency for TES to overestimate surface canopy temperature as a result of underestimation of emissivity, and that current TES retrievals have RMSE values within the range of literature values for vegetated surfaces. The addition of AVIRIS derived water vapor improved retrieval accuracy as expected, although still not to within a kelvin of true canopy temperature.

The WVS method showed significant improvement over TES, both with and without the addition of per pixel water vapor. In contrast to TES retrievals, the

Table 3.1: Comparison of temperature retrievals from remote sensing data with field validation data. RMSE values are calculated relative to corrected LiCor field measurements, and are weighted according to the number of observations occurring within the corresponding pixel. The JPL standard TES product is representative of current (2014) operational retrievals performed by NASA for ASTER, MODIS, and MASTER instruments, and is used as our baseline when comparing percent error reduction between temperature retrieval methods.

		Corrected LiCor leaf temperature	**Single-band inversion** *AVIRISWV*		**Temperature Emissivity Separation** *JPL Standard*		*AVIRISWV*		**Water Vapor Scaling** *NCEP*		*AVIRISWV*	
Vine	*N Obs*	*meantemp*	*temp*	*resids*	*temp*	*resids*	*temp*	*resids*	*temp*	*resids*	*temp*	*resids*
48	3	308.46	309.06	-0.60	311.70	-3.24	310.14	-1.68	309.60	-1.14	308.97	-0.51
21	2	309.52	309.25	0.27	311.19	-1.67	310.25	-0.73	309.76	-0.24	309.59	-0.07
25	2	309.78	309.81	-0.03	311.34	-1.56	310.83	-1.05	309.49	0.29	309.33	0.45
13	1	309.70	309.26	0.44	310.90	-1.20	310.61	-0.91	309.51	0.19	309.29	0.41
16	1	310.88	312.45	-1.57	314.07	-3.19	314.05	-3.17	312.35	-1.47	312.28	-1.40
10	2	311.24	312.15	-0.91	314.10	-2.86	313.06	-1.82	311.65	-0.41	311.40	-0.16
8	2	311.73	312.19	-0.46	313.87	-2.14	313.44	-1.71	311.92	-0.19	311.80	-0.07
1	1	311.98	312.24	-0.26	313.52	-1.54	313.46	-1.48	312.03	-0.05	311.91	0.07
NObs Weighted RMSE (K)			0.66		2.41		1.63		0.70		0.49	
% error reduction			72.8%		–		32.3%		71.1%		79.6%	

small errors that are present for the WVS method are distributed both above and below the reference temperatures, further strengthening our confidence that these retrievals are not biased. Coarse scale NCEP water vapor data (1 degree) still yielded well under a kelvin RMSE, an over 70% reduction in error from the current JPL product that WVS will replace. The addition of AVIRIS water vapor to the WVS method saw still further gains in accuracy, reducing retrieval RMSE to under a half kelvin. The WVS temperature retrievals are shown in Figure 3.1, with the spatial north-south temperature gradient from the different watering regimes clearly visible, and additional spatial detail present in the retrieval that incorporated the AVIRIS derived water vapor.

3.1 Separation of Atmospheric and ϵ_λ Errors

Some insight into the major source of errors when applying the TES method can be inferred from the high accuracy that the single band inversion method offers in cases where the prescribed ϵ is close to the true emissivity. Since the emissivity for one band is prescribed *a priori* in single band inversion, for surfaces that have emissivities close to this prescribed value such as vegetation, we can expect that the major source of error will be from the atmospheric $L_\lambda^\uparrow$, $L_\lambda^\downarrow$, and τ_λ terms. Both single band inversion and one of the TES retrievals share identical per pixel values

of $L_\lambda^\uparrow$, $L_\lambda^\downarrow$, and τ_λ—with the TES retrieval actually decreasing in accuracy after calibrating emissivities. We see here small errors in atmospheric error propagating to larger errors in emissivity (usually ϵ_λ underestimation), ultimately resulting in higher temperature error due to emissivity estimation opposed to atmospheric path radiance residuals in the Planck inversion.

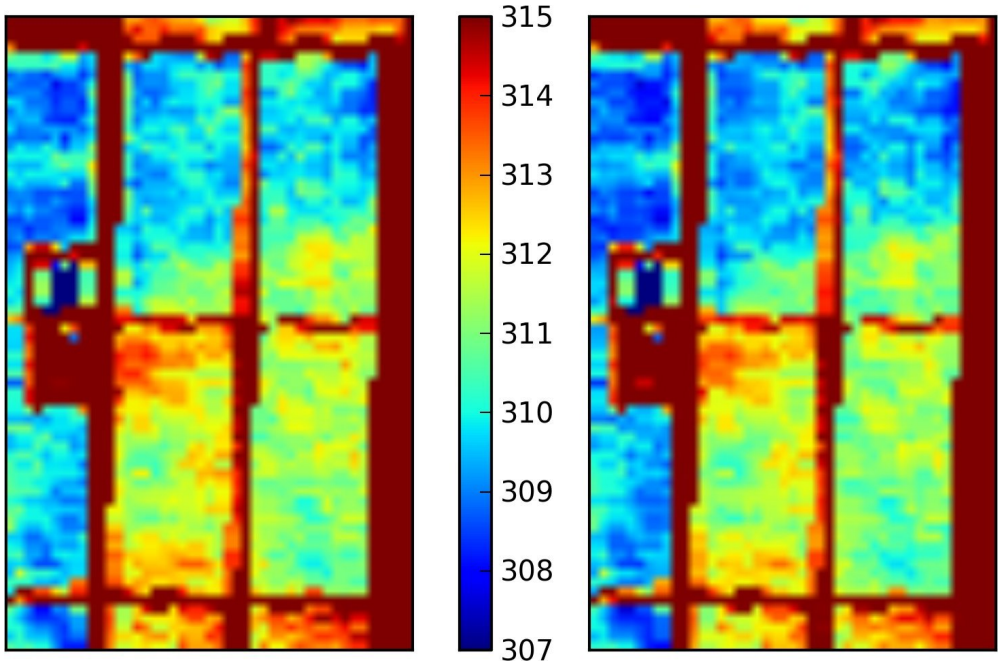

Figure 3.1: Temperature retrieval (units kelvin) over Delano Vineyards from the WVS method with AVIRIS water vapor (*right*) and without (*left*)

Chapter 4

Discussion

The results of this study highlights our ability to correct for atmospheric sources of error in the TIR when retrieving canopy temperature. Canopy temperature is a crucial physiologic state variable that governs gas exchange with the atmosphere, and controls gross photosynthesis by limiting or enhancing carbon uptake, transpiration, and respiration. Retrieving canopy temperature at sub-kelvin accuracy allows farmers and scientists to assess when vegetation respiration is increasing faster than photosynthesis, quantify the total hydrologic exchange with the atmosphere, and pinpoint heat stress that directly reduces photosynthesis rates due to enzyme inactivation. At the field scale, accurate canopy temperature measurements are crucial to efficient water use in agriculture where transpiration rates are used to assess water loss to the atmosphere; at regional spatial scales, canopy temperature maps heat damage and forecasts yield reduction or failure in

crops, and also provides insight into the respiration rates of heterogenous natural biomes.

4.1 Spatial Patterns

The dominate pattern of observed canopy temperatures in Figure 3.1 shows the effects of different watering regimes in the North and South blocks. Additional fine scale spatial variability of temperature within the field are likely the result of pressure drops in the irrigation line, differences in soil composition and hydrologic capacity, and/or other plant physiologic stresses such as pest infestation, disease or nutrient stress. The observed canopy temperature range at the vineyard—up to 8 kelvin between the North and South blocks, and over 5 kelvin within a single block—has substantial implications for productivity. Previous studies of woody vegetation have found that a difference of 7 to 8 kelvin in canopy temperature corresponds to the difference between peak photosynthesis and photosynthesis at 75% of peak (Larcher 1969). Since plants reduce fruit production when stressed, the reduction of gross photosynthesis has an outsized impact on harvest yield; for the Delano field site the reduction in yield in the 2011 experiment required that experiments the following year use a less aggressive water reduction.

4.2 Implications for the HyspIRI mission

We show a definitive and substantial improvement in temperature retrievals when synthesizing TIR and SWIR instruments, and offer a preview of the accuracy HyspIRI will provide over vegetated surfaces using the WVS method proposed by JPL. Comparison of WVS applied both with and without hyperspectral derived water vapor quantifies the improvement we can expect from the portion of the TIR and SWIR instruments that will overlap, and hints at potential along the edges where they do not.

Vegetated surfaces are typically challenging targets for temperature inversion, and accurate temperature retrieval of these surfaces bodes well for our ability to invert less challenging surfaces that have greater spectral contrast. Regardless of surface type, the degree of temperature retrieval improvement with the WVS method can be expected to scale, with greater improvements in areas more humid than the central valley. Given that the majority of water vapor occurs below the altitude of our flight lines, and the similarity of the MASTER instrument to the proposed HyspIRI instrument, it is reasonable to expect similar canopy temperature accuracy from HyspIRI over closed canopies in areas such as the central valley, with increasing surface temperature retrieval accuracy for heterogenous non-greybody pixels such as playas and water.

While the synthesis of hyperspectral derived water vapor and TIR data will only be possible for the 150km swath of the HyspIRI VSWIR instrument (as opposed to the 600km TIR radiometer swath), the technique remains a powerful option to use over complex terrains with a high degree of spatial variability in column water vapor. Since total precipitable water vapor is strongly correlated with elevation, the relative improvements that we observed when using hyperspectral derived water vapor in place of NCEP provided water vapor are likely conservative for what we can expect in areas of greater topographic variability than the central valley.

The improved temperature retrievals we demonstrate using WVS over gray-body pixels is dominated by a reduction in propagated error in estimating surface emissivity—a result that portends a future for the HyspIRI mission focused on other, non-atmospheric challenges. Chief among these challenges will likely be the scaling issues inherent in estimating canopy scale physical phenomena using a 60 meter HyspIRI pixel. Orchard cash crops such as almonds and pistachios present a multisource emission target, as do pixels that cover multiple adjacent plots—and all of which will require multimember definitions of surface temperature to be meaningful. Ultimately, further refinement of temperature estimates will require modeling endmember fractions and thermal unmixing of the fractional surface cover that accounts for varying endmember emissivity and temperature.

The HyspIRI mission will be well equipped to accomplish the former using established mixture analysis methods in the VSWIR, however the latter will necessitate dealing with substantial nonlinearities present in TIR mixing.

One possible approach for future studies that aim to tackle this unmixing challenge is to modify the split-window approach. The split-window approach pioneered by Dozier (1981) solves for endmember fractions and temperature simultaneously, given known endmember emissivities. Since hyperspectral measurements can provide accurate fractional cover estimates, direct inversion of emissivity from WVS corrected radiant emission and endmember fractions may be possible within an error minimization framework that uses total at sensor radiance as way to constrain the solution space.

Bibliography

Allen, R. G., Pereira, L. S., Raes, D., Smith, M. et al. (1998), 'Crop evapotranspiration-Guidelines for computing crop water requirements-FAO Irrigation and drainage paper 56', *FAO, Rome* **300**, 6541.

Alsina, M., Cheng, T., Riaño, D., Whiting, M., Ustin, S. & Smart, D. (2013), Water status detection in California table grapes: from leaf to airborne, *in* 'Precision agriculture'13', Springer, pp. 225–231.

Baldridge, A., Hook, S., Grove, C. & Rivera, G. (2009), 'The ASTER spectral library version 2.0', *Remote Sensing of Environment* **113**(4), 711–715.

Berk, A., Anderson, G. P., Acharya, P. K., Bernstein, L. S., Muratov, L., Lee, J., Fox, M., Adler-Golden, S. M., Chetwynd, J. H., Hoke, M. L. et al. (2005), Modtran 5: a reformulated atmospheric band model with auxiliary species and practical multiple scattering options: update, *in* 'Defense and Security', International Society for Optics and Photonics, pp. 662–667.

Berk, A., Bernstein, L., Anderson, G., Acharya, P., Robertson, D., Chetwynd, J. & Adler-Golden, S. (1998), 'Modtran cloud and multiple scattering upgrades with application to aviris', *Remote Sensing of Environment* **65**(3), 367–375.

Berk, A., Bernstein, L. S. & Robertson, D. C. (1987), MODTRAN: A moderate resolution model for LOWTRAN, Technical report, DTIC Document.

Carrère, V. & Conel, J. E. (1993), 'Recovery of atmospheric water vapor total column abundance from imaging spectrometer data around 940 nm — sensitivity analysis and application to Airborne Visible/Infrared Imaging Spectrometer (AVIRIS) data', *Remote Sensing of Environment* **44**(2-3), 179–204.
URL: *http://dx.doi.org/10.1016/0034-4257(93)90015-p*

CDFA (2013), Agricultural Statistical Review, Technical report, California Department of Food and Agriculture, Sacramento CA.

Dozier, J. (1981), 'A method for satellite identification of surface temperature fields of subpixel resolution', *Remote Sensing of environment* **11**, 221–229.

Gao, B.-C. & Goetz, A. F. H. (1990), 'Column atmospheric water vapor and vegetation liquid water retrievals from Airborne Imaging Spectrometer data', *Journal of Geophysical Research* **95**(D4), 3549.
URL: *http://dx.doi.org/10.1029/jd095id04p03549*

Gillespie, A., Rokugawa, S., Matsunaga, T., Cothern, J., Hook, S. & Kahle, A. (1998), 'A temperature and emissivity separation algorithm for Advanced Spaceborne Thermal Emission and Reflection Radiometer (ASTER) images', *IEEE Transactions on Geoscience and Remote Sensing* **36**(4), 1113–1126.
URL: *http://dx.doi.org/10.1109/36.700995*

Green, R., Conel, J., Margolis, J., Bruegge, C. & Hoover, G. (1991), An inversion algorithm for retrieval of atmospheric and leaf water absorption from AVIRIS radiance with compensation for atmospheric scattering, *in* 'Annual JPL Airborne Visible/Infrared Imaging Spectrometer (AVIRIS) Workshop', Vol. 3, pp. 91–28.

Green, R. O., Conel, J. E. & Roberts, D. A. (1993), '¡title¿Estimation of aerosol optical depth, pressure elevation, water vapor, and calculation of apparent surface reflectance from radiance measured by the airborne visible/infrared imaging spectrometer (AVIRIS) using a radiative transfer code¡/title¿', *Imaging Spectrometry of the Terrestrial Environment* .
URL: *http://dx.doi.org/10.1117/12.157054*

Gustafson, W. T., Gillespie, A. R. & Yamada, G. J. (2006), Revisions to the ASTER temperature/emissivity separation algorithm, *in* '2nd international symposium on Recent Advances in Quantitative Remote Sensing'.

Hook, S. J., Myers, J. J., Thome, K. J., Fitzgerald, M. & Kahle, A. B. (2001), 'The MODIS/ASTER airborne simulator (MASTER) — a new instrument for earth science studies', *Remote Sensing of Environment* **76**(1), 93–102.
URL: *http://dx.doi.org/10.1016/s0034-4257(00)00195-4*

Howitt, R., Medellin-Azuara, J. & Lund, J. (2014), 'Preliminary 2014 Drought Economic Impact Estimates in Central Valley Agriculture'.

Hulley, G. C. (2011), *HyspIRI Level-2 Thermal Infrared (TIR) land surface temperature and emissivity algorithm theoretical basis document*, Pasadena, CA: Jet Propulsion Laboratory, National Aeronautics and Space Administration.

Hulley, G. C. & Hook, S. J. (2009), 'The North American ASTER land surface emissivity database (NAALSED) version 2.0', *Remote Sensing of Environment* **113**(9), 1967–1975.

Hulley, G. C., Hughes, C. G. & Hook, S. J. (2012), 'Quantifying uncertainties in land surface temperature and emissivity retrievals from ASTER and MODIS thermal infrared data', *J. Geophys. Res.* **117**(D23).
URL: *http://dx.doi.org/10.1029/2012jd018506*

Hulley, G. & Hook, S. (2011), 'HyspIRI Level-2 TIR surface radiance algorithm theoretical basis document'.

Hulley, G., Veraverbeke, S. & Hook, S. (2014), 'Thermal-based techniques for land cover change detection using a new dynamic modis multispectral emissivity product (mod21)', *Remote Sensing of Environment* **140**, 755–765.

Jackson, R. D., Idso, S., Reginato, R. & Pinter, P. (1981), 'Canopy temperature as a crop water stress indicator', *Water resources research* **17**(4), 1133–1138.

Jarvis, P. & McNaughton, K. (1986), 'Stomatal Control of Transpiration: Scaling Up from Leaf to Region', *Advances in Ecological Research* p. 1–49.
URL: *http://dx.doi.org/10.1016/s0065-2504(08)60119-1*

Larcher, W. (1969), 'Effect of environmental and physiological variables on the carbon dioxide gas exchange of trees', *Photosynthetica* .

Matsunaga, T. (1994), 'A temperature-emissivity separation method using an empirical relationship between the mean, the maximum, and the minimum of the thermal infrared emissivity spectrum', *Jour. Remote Sens. Soc. Japan* **14**(2), 230–241.

Monteith, J. et al. (1965), Evaporation and environment, *in* 'Symp. Soc. Exp. Biol', Vol. 19, p. 4.

Nelder, J. A. & Mead, R. (1965), 'A Simplex Method for Function Minimization', *The Computer Journal* **7**(4), 308–313.
URL: *http://dx.doi.org/10.1093/comjnl/7.4.308*

Realmuto, V. (1990), Separating the effects of temperature and emissivity: Emissivity spectrum normalization, *in* 'Proc. 2nd TIMS Workshop', pp. 90–55.

Roberts, D. A., Quattrochi, D. A., Hulley, G. C., Hook, S. J. & Green, R. O. (2012), 'Synergies between VSWIR and TIR data for the urban environment:

An evaluation of the potential for the Hyperspectral Infrared Imager (HyspIRI) Decadal Survey mission', *Remote Sensing of Environment* **117**, 83–101.
URL: *http://dx.doi.org/10.1016/j.rse.2011.07.021*

Scheele, C., Rill, L., Grigsby, S. & Ustin, S. (2013), Land Surface Temperature Retrieval Through the Synthesis of Hyperspectral and Multispectral Data from the HyspIRI Preparatory Flight Campaign, *in* 'AGU Fall Meeting Abstracts', Vol. 1, p. 0457.

Tonooka, H. (2001), 'An atmospheric correction algorithm for thermal infrared multispectral data over land-a water-vapor scaling method', *Geoscience and Remote Sensing, IEEE Transactions on* **39**(3), 682–692.

Tonooka, H. (2005), 'Accurate atmospheric correction of ASTER thermal infrared imagery using the WVS method', *Geoscience and Remote Sensing, IEEE Transactions on* **43**(12), 2778–2792.

Zhengming, W. & Dozier, J. (1989), 'Land-surface temperature measurement from space: physical principles and inverse modeling', *IEEE Transactions on Geoscience and Remote Sensing* **27**(3), 268–278.
URL: *http://dx.doi.org/10.1109/36.17668*